Soft Matter

PAPER

View Article Online
View Journal | View Issue

Cite this: *Soft Matter*, 2022, **18**, 6582

Force-driven active dynamics of thin nanorods in unentangled polymer melts†

Siteng Zhang, Jiuling Wang and Ting Ge *

Recent advances in the functional material and biomedical applications of nanorods call for a fundamental understanding of the active motion of nanorods in a viscoelastic medium. Molecular dynamics simulations are performed to investigate a model system consisting of force-driven active thin nanorods in a melt of unentangled polymers. The activeness of a thin nanorod arises from a constant external force applied uniformly along the rod. The simulations demonstrate that the active force overcomes the randomness of the diffusive motion and results in a ballistic motion along the direction of the applied force at long timescales. The constant speed of the force-driven ballistic motion is determined by the balance of the active force and the friction from the coupling of the nanorod with the polymer viscosity. The friction coefficient, which is computed as the ratio of the active force and the speed, decreases as the active force increases. The origin of the reduction in the friction coefficient is the high speed that allows the nanorod to renew its local environment faster than the relaxation time of melt chains. A scaling theory is developed to quantify the dependence of the friction coefficient on the strength of the active force. The simulations also demonstrate that the force-driven ballistic motion suppresses the rotational diffusion of the rod and cuts off the de-correlation of the rod axis with time. On the scaling level, the long-time trajectory of a force-driven active nanorod piercing through unentangled polymers may be described as a stretched array of "active blobs", where the short-time random-walk trajectory within an active blob is unperturbed by the active force.

Received 2nd June 2022,
Accepted 6th August 2022

DOI: 10.1039/d2sm00731b

rsc.li/soft-matter-journal

1 Introduction

The dynamics of nanorods in a viscoelastic medium are critical to many applications of nanorods. The fabrication and processing of nanorod-containing polymer composites, which possess tunable mechanical,[1–4] optical,[5–7] and electrical[8–12] properties, are affected by the dynamics of nanorods. The uses of nanorods as diagnostic probes in bio-imaging[13–16] and as drug delivery vehicles in bio-medicine[17–26] rely on the dynamics of nanorods in a complex environment of biological molecules.[27] With thermal agitation, the dynamics of nanorods are passive and coupled with the viscoelasticity of surrounding molecules, exhibiting the random nature of Brownian motion.[28–32] Going beyond the randomness of passive dynamics, the active dynamics of nanorods may be induced either by an external field such as a magnetic field,[18,33] an electric field,[34] near-infrared light[18] and ultra sound[20,23] or by a chemistry-based mechanism of self-propulsion.[17,35–39] A fundamental understanding of the active motion of nanorods in a viscoelastic medium will benefit further advances in the material and biomedical applications of nanorods.

The passive dynamics of thin nanorods in viscoelastic polymers are characterized by a length-scale- and shape-dependent breakdown of the Stokes-Einstein relation in the continuum theory.[40] The diffusion coefficients for different modes of the nanorod dynamics, including the translational motion along and normal to the rod axis, the overall translational motion, and the rotational motion of the rod axis, are all related to the bulk viscosity of surrounding molecules in the Stokes–Einstein relation.[41,42] Nevertheless, recent experiments[28,29] and computer simulations[30,31,43] have revealed the coupling of a nanorod only to a fraction of the bulk viscosity, indicating the breakdown of the Stokes–Einstein relation. Molecular dynamics simulations of monomerically thin nanorods in unentangled polymer melts[43] have shown the anisotropy in the translational diffusion along and normal to the rod axis. The parallel diffusion in the body frame of the thin nanorod is coupled to the local viscosity on the monomer length scale, which is independent of the rod length l. The coupling to the local monomeric viscosity reflects a full screening of the hydrodynamic interactions. By contrast, the normal diffusion is coupled with an effective viscosity that depends on l with respect to the polymer chain size, corresponding to unscreened hydrodynamic interactions. The same

Department of Chemistry and Biochemistry, University of South Carolina, Columbia, South Carolina 29208, USA. E-mail: tingg@mailbox.sc.edu

† Electronic supplementary information (ESI) available. See DOI: https://doi.org/10.1039/d2sm00731b

effective viscosity for the normal diffusion also dictates the rotational diffusion of the rod axis. For the overall translational diffusion in the lab frame, the effective viscosity corresponds to a partial screening of the hydrodynamic interactions, as both the parallel and normal components contribute to the overall diffusion.

Activeness is anticipated to alter the interplay between the nanorods and the viscoelasticity of the surrounding medium, as the ballistic motion induced by the activeness has been shown to enhance the mobility of nanoscale objects in experiments[27] and computer simulations.[44,45] To investigate the active dynamics of nanorods in a viscoelastic medium, we perform molecular dynamics simulations and scaling analysis of a model system consisting of force-driven active thin nanorods in a melt of unentangled polymers. The thickness of the nanorod is comparable to the monomer size, and the aspect ratio of the nanorod is ≥ 4. The unentangled polymer chains represent a viscoelastic medium with internal chain relaxation dynamics. The activeness of a thin nanorod is introduced by applying an active force uniformly along the initial rod axis, which facilitates the arrival of the steady state in the simulations. We find that the active force overcomes the randomness of the diffusive motion and results in a ballistic motion of the thin nanorod along the force direction at long timescales. The constant speed of the force-driven ballistic motion is determined by the balance of the active force and the friction from the coupling of the nanorod with the polymer melt. The friction coefficient decreases as the strength of the active force increases. We determine the origin of the reduction in the friction coefficient is the fact that the high speed renews the local environment of the nanorod faster than the relaxation time of polymer chains. We develop a scaling theory that successfully describes the dependence of the friction coefficient on the strength of the active force as well as the onset of the reduction in the friction coefficient in the simulations. We also find that the active force suppresses the rotational diffusion of the rod and cuts off the de-correlation of the rod axis with time.

2 Models and methods

We simulate the polymers using the canonical bead-spring model.[46–48] Monomers of size σ and mass m interact *via* the Lennard-Jones (LJ) potential with an interaction strength ε, cut-off distance $r_c = 2.5\sigma$, and unit time $\tau = \sigma\sqrt{m/\varepsilon}$. Polymer chains of N monomers each are connected by the finitely extensible nonlinear elastic (FENE) bonds. We simulate the thin nanorods as rigid bodies made of beads identical to the monomers. To create a thin nanorod of length l, l/σ beads are placed along a straight line with regular spacing σ and grouped into a rigid body. The interaction between a bead of a nanorod and a surrounding monomer is the weakly attractive LJ potential with $r_c = 2.5\sigma$, which promotes the dispersion of nanorods in the melt. The interaction between two beads from two different nanorods is the purely repulsive LJ potential with $r_c = 2^{1/6}\sigma$, which prevents the aggregation of the nanorods.

Nanorods and polymers were placed in a cubic box with side length L and periodic boundary conditions in all three directions. Each sample was equilibrated at temperature $T = 1.0\varepsilon/k_B$ and pressure $P = 0$. The equilibration was performed with a Nosé–Hoover thermostat/barostat applied to the polymer chains. A Nosé–Hoover thermostat was applied to both the translational and rotational degrees of freedom of the rigid nanorods. The characteristic damping time of the thermostat was 10τ, and that of the barostat was 100τ. The equilibration run lasted for a time that is much longer than the diffusion time of the polymer chains. There are two sets of simulation samples. In one set, the polymer chain length $N = 16$, and the rod length $l = 4\sigma$, 8σ, 16σ, and 32σ. In the other set, $N = 64$, while $l = 4\sigma$, and 8σ. The first set corresponds to l comparable to and larger than the root-mean-squared end-to-end size of the polymer chain, $R = 4.7\sigma$. The second set corresponds to $l < R = 10.1\sigma$. In all samples, the number of nanorods is $N_r = 27$, while the number of polymer chains N_c varies. Multiple nanorods are simulated simultaneously for a better statistical average of the dynamics data. As shown in Table 1, the volume fraction of the nanorods $\phi_r = N_r l\sigma^2/L^3$ is less than 0.07%, and the volume fraction of the excluded volume $\phi_{exl} = N_r l^2\sigma/L^3$ is less than 2.1% in all samples. Recently, it has been shown that the organization of nanorods in polymer nanocomposites depends on the details of the nanorod model.[49,50] For the specific models of nanorods and polymers used here and the low volume fraction of nanorods in the simulations, we have confirmed that the nanorods are well dispersed without any aggregation in all samples.[43] Additionally, because of the low volume fraction of nanorods in the simulations and the lack of a theory for the long-range correlation of nanorod pairs, we do not attempt to quantify and correct for the effects of any long-range pair correlation on the dynamics of individual nanorods.

The dynamics of nanorods in polymer melts were simulated at a fixed volume and a constant temperature $T = 1.0\varepsilon/k_B$. The temperature of polymer chains was controlled using a Nosé–Hoover thermostat with a characteristic damping time of 10τ. The activeness of a nanorod was modeled by applying a constant active force along the initial rod axis such that the driven motion of the nanorod along the active force direction is commensurate with the preferential thermal diffusion of the nanorod along the rod axis,[43] facilitating the arrival of the steady state in the simulations. The active force is uniformly distributed along the rod with each bead subjecting to an active force $f_0^a\mathbf{u}(0)$, where $\mathbf{u}(0)$ is the unit vector along the initial rod axis. Fig. 1

Table 1 Parameters for the simulations of force-driven active thin nanorods in unentangled polymer melts

Chain length N	Num. of chains N_c	Box size L (σ)	Nanorod length l (σ)	Num. of rods N_r	Vol. fraction ϕ_r (%)	Excluded vol. fraction ϕ_{exl} (%)
16	73 818	110.5	4	27	0.008	0.032
16	73 818	110.5	8	27	0.016	0.128
16	73 818	110.5	16	27	0.032	0.512
16	73 818	110.5	32	27	0.064	2.048
32	36 909	110.2	4	27	0.032	0.516
32	36 909	110.2	8	27	0.065	2.065

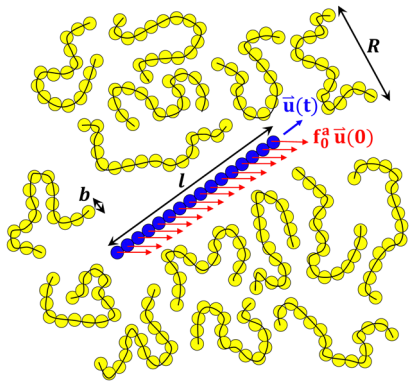

Fig. 1 Schematic illustration of a force-driven active thin nanorod (a rigid body of blue spheres) in a melt of unentangled polymers (yellow spheres connected by black lines). The monomer size b, rod length l, and melt chain size R are indicated. The active force is applied uniformly along the rod with a magnitude of f_0^a per monomer length. The active force is along the initial rod axis with unit vector $\vec{u}(0)$, while the orientation of the rod axis changes over time with a time-dependent unit vector $\vec{u}(t)$.

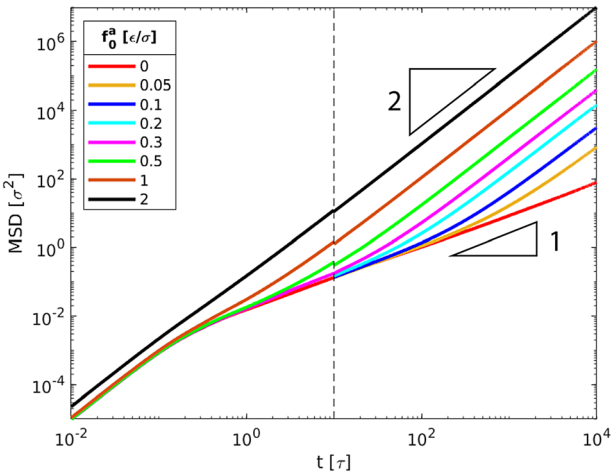

Fig. 3 MSD$\langle \Delta r^2(t) \rangle$ of the force-driven active thin nanorods with length $l = 32\sigma$ and indicated active force per monomer f_0^a in a melt of polymer chains with $N = 16$ monomers per chain. $f_0^a = 0$ corresponds to the passive dynamics of thin nanorods with no activeness. Dashed line indicates $t = 10\tau$ that separates two independent computations of MSDs for $t < 10\tau$ and $10 \leq t \leq 10^4\tau$.

illustrates a force-driven active thin nanorod in an unentangled polymer melt. f_0^a varied from 0 to $2.0\varepsilon/\sigma$. To enable the activeness, no thermostat was applied to the thin nanorods. The time step for integrating the equations of motion was 0.01τ. The net linear momentum and net angular momentum of the polymer melt were zeroed after each step of integration, so there was no drift or rotation of the melt. All simulations were performed using the LAMMPS simulation package.[51,52]

3 Results and discussion

Representative trajectories for the dynamics of active nanorods in the simulations are shown in Fig. 2. The dynamics of an active nanorod is quantified by the mean-square displacement (MSD) $\langle \Delta r^2(t) \rangle = \langle [\vec{r}_{com}(t) - \vec{r}_{com}(0)]^2 \rangle$ of the center of mass of the nanorod as a function of time t in the polymer melts. Fig. 3 shows $\langle \Delta r^2(t) \rangle$ for the nanorods of $l = 32\sigma$ in the polymers of $N = 16$ with increasing f_0^a. $\langle \Delta r^2(t) \rangle$ for $t < 10\tau$ and $10\tau \leq t \leq 10^4\tau$ are computed separately. Depending on the strength of the active force, the production run for MSD in the time window $10\tau < t < 10^4\tau$ lasted from $4 \times 10^4\tau$ to $6 \times 10^5\tau$. Coordinates were dumped every 10τ. For the earlier time window $0.01\tau < t < 10\tau$, the production run lasted for 100τ, and coordinates were dumped every 0.01τ in all cases. In the calculations of MSD, the average was taken over different nanorods and different time periods of the same length in the steady state.

The scenario with $f_0^a = 0$ corresponds to the passive dynamics of nanorods. The corresponding MSD exhibits a crossover from the initial thermal ballistic motion with $\alpha = d \log\langle \Delta r^2(t) \rangle / d \log t = 2$ to the sub-diffusive motion with $\alpha < 1$ at intermediate timescales and eventually to the terminal diffusion with $\alpha = 1$, in agreement with the previous simulation result.[43] For $f_0^a > 0$,

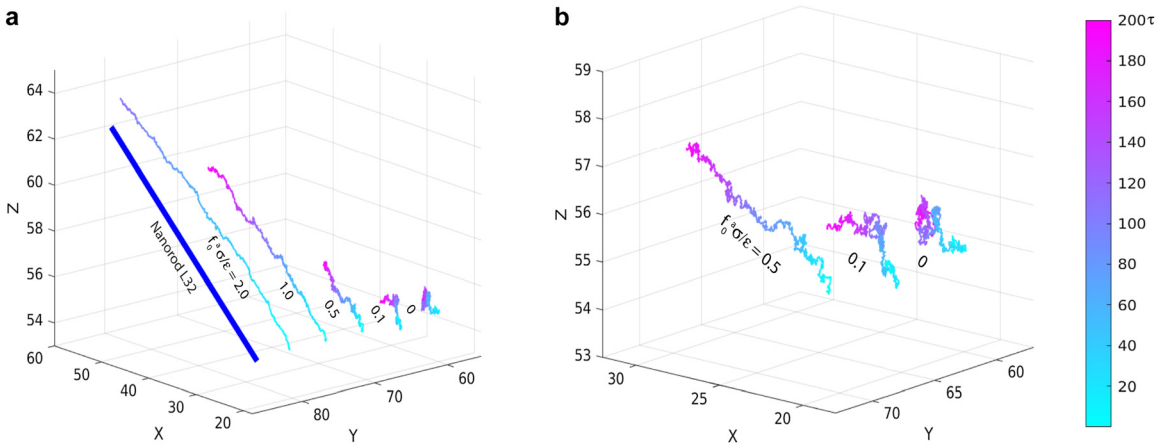

Fig. 2 (a) Molecular dynamics trajectories of force-driven active thin nanorods of length $l = 32\sigma$ in polymer melts of chain length $N = 16$ at indicated magnitudes of active force. Three trajectories in (a) are enlarged and shown in (b). For the trajectory at the strongest active force $f_0^a = 2\varepsilon/\sigma$, only the part comparable to the rod length is shown.

the MSD is characterized by the new force-driven ballistic regime with $\alpha = 2$ at long timescales. The overlap of the MSD for the active nanorods prior to the force-driven ballistic regime with the MSD for the passive dynamics of nanorods indicates that the active force is not sufficiently strong such that the nanorod dynamics are dictated by the thermal motion at short timescales. With increasing f_0^a, the force-driven ballistic regime begins at a shorter time. Eventually, for the largest $f_0^a = 2\varepsilon/\sigma$, the force-driven ballistic regime covers the entire range of timescales explored in the simulations.

For the simulation samples in Fig. 3, we further decomposed the overall MSD into two components that are parallel and normal to the direction of the applied force, respectively. Note that the direction of the force, which is aligned with the initial rod axis, is fixed in the lab frame. The results from the decomposition are presented as ESI.† The parallel component is almost identical to the overall MSD in the force-driven ballistic regime, indicating the force-driven ballistic motion is along the force direction. The normal component exhibits rich time-dependent features that need further study, but its contribution to the overall MSD in the force-driven ballistic regime is very minor. See ESI† for a more detailed discussion.

In all cases, the force-driven ballistic motion is quantified by a constant speed v^a, which is computed from the long-time value of $\sqrt{\langle \Delta r^2(t)\rangle/t^2}$. The increase of v^a with increasing f_0^a for the samples in Fig. 3 is shown in Fig. 4. v^a for $f_0^a = 2\varepsilon/\sigma$ is slightly above the thermal speed of the nanorod with 32 beads of mass m, which is $v^{\text{thermal}} = \sqrt{3k_BT/32m} = 0.31\sigma/\tau$. $v^a > v^{\text{thermal}}$ indicates that the ballistic motion dominates the thermal motion at all timescales, as the displacement $v^a t$ from the active motion is sufficiently large that it surpasses the displacement $v^{\text{thermal}}t$ from the undamped thermal ballistic motion. The increase of v^a with increasing f_0^a can also be observed in the representative trajectories of active nanorods in Fig. 2, where the displacement over the same time of 200τ increases with increasing f_0^a.

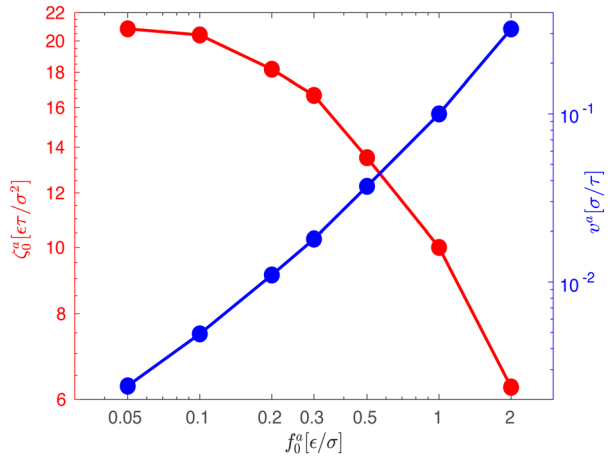

Fig. 4 The speed v^a for the force-driven ballistic motion (right axis) and the monomeric friction coefficient $\zeta_0^a = f_0^a/v^a$ (left axis) as functions of the active force per monomer f_0^a for the same systems in Fig. 3.

As the speed v^a increases with the strength of the active force, the friction coefficient for the force-driven ballistic motion of an active nanorod decreases. In the force-driven ballistic regime, there is a balance between the active force $f_0^a(l/\sigma)$ and the frictional force $\zeta^a v^a$, where ζ^a is the friction coefficient. From $f_0^a(l/\sigma) = \zeta^a v^a$, the monomeric friction coefficient $\zeta_0^a = \zeta^a/(l/\sigma) = f_0^a/v^a$. The dependence of ζ_0^a on f_0^a for the simulation samples in Fig. 3 is shown in Fig. 4. In the limit of vanishing f_0^a, ζ_0^a approaches a plateau that corresponds to the passive dynamics of the nanorod, for which the monomeric friction coefficient is $\zeta_0 = 22.5\varepsilon\tau/\sigma^2$.[43] As f_0^a increases, ζ_0^a deviates from ζ_0 and decreases as the force-driven ballistic motion dominates over the thermal motion at decreasing timescale.

To understand the dynamics of an active nanorod in unentangled polymers, we develop a scaling theory. Consider a nanorod of length l and thickness comparable to the Kuhn monomer size b in a polymer melt. Each polymer consists of N monomers, and the polymer chains are unentangled. The active force along the initial rod axis is f_0^a per monomer. Refer to Fig. 1 for a schematic illustration of the force-driven nanorod in polymer chains.

We first review the scaling description of the passive dynamics of the nanorods with $f_0^a = 0$ in unentangled polymers. The nanorod in diffusion experiences an effective viscosity η_{eff} that is comparable to the geometric mean of the viscosity η_0 on the monomer length scale and the maximum viscosity $\eta_{\max}$ that the rod can experience. The scaling relation $\eta_{\text{eff}} \approx (\eta_0\eta_{\max})^{1/2}$ corresponds to a partial screening of the hydrodynamic interactions in the coupling between the nanorod and the melt. Note that if $\eta_{\text{eff}} \approx \eta_0$ and $\eta_{\text{eff}} \approx \eta_{\max}$, there is a full screening and no screening of the hydrodynamic interactions beyond the monomer length scale, respectively. When l is larger than the average size $R \approx N^{1/2}b$ of the melt chain in the random-walk conformation, $\eta_{\max}$ for unscreened hydrodynamic interactions is comparable to the melt viscosity $\eta_{\text{melt}} \approx \eta_0 N$. However, when $l < R$, $\eta_{\max}$ is instead only comparable to the viscosity $\eta_g \approx \eta_0 g \approx \eta_0(l^2/b^2)$ of local chain segments, which contain g monomers in each segment and have an average chain size $g^{1/2}b \approx l$.

A length-scale dependent η_{eff} has been used to describe the diffusion of spherical nanoparticles in various polymer systems,[40,53–57] and it is consistent with the length-scale dependent nanoparticle dynamics in alternative theoretical approach.[58–60] For nanorods, the rule of geometric mean reflects the additional effects of the anisotropic particle shape on η_{eff}. While the diffusion along the rod axis is determined by the monomeric viscosity η_0, the diffusion normal to the rod axis is determined by $\eta_{\max}$. Such a difference between the parallel and normal components with respect to the rod axis, *i.e.*, in the body frame, has been shown by the recent simulations on the diffusion of nanorods.[43] The rule of geometric mean composites the viscosity for the diffusion parallel and normal to the rod axis to obtain η_{eff} for the diffusion in the lab frame. The rule was first used by Aponte-Rivera and Rubinstein[61] in the scaling theory for the dynamical coupling in oppositely charged polyelectrolytes, where η_{eff} for the polyanion correlation segments is the geometric mean of the values for the full screening and no

screening of the hydrodynamic interactions. Note that in the theoretical description throughout the paper, $\approx$ indicates the equation is on the scaling level with an order-of-unity coefficient dropped.

The friction coefficient for the passive dynamics of a nanorod $\zeta \approx \eta_{\text{eff}} l$, and the diffusion coefficient $D = k_B T/\zeta$, according to the Stokes law and Einstein relation, respectively. As a result, the MSD is $\langle \Delta r^2(t) \rangle \approx Dt \approx (k_B T/\eta_{\text{eff}} l)t$ in the terminal diffusive regime. If $l \geq R$, the time scale τ_d at which the terminal diffusion begins is comparable to the relaxation time of the melt τ_{melt}. Using the N-dependence of the relaxation time in the Rouse dynamics model,[41] $\tau_{\text{melt}} \approx \tau_0 N^2$, where τ_0 is the monomeric time scale. If $l < R$, τ_d is comparable to the Rouse time of the g-monomer segments, $\tau_g \approx \tau_0 g^2 < \tau_{\text{melt}}$.

For a force-driven active nanorod, the friction coefficient ζ^a is comparable to ζ in the limit of vanishing f_0^a, as shown by the simulation result in Fig. 4. The force-driven ballistic motion of an active nanorod with a small speed v^a begins at a time scale $\tau^a_{\text{ballistic}} > \tau_d$, where the motion of a passive nanorod with $f_0^a = 0$ is already in the terminal diffusive regime. The ballistic motion with $\tau^a_{\text{ballistic}} > \tau_d$ renews the local environment of the nanorod sufficiently slow such that the relaxation dynamics that determine the thermal diffusion of the passive nanorod is complete. As a result, the same friction that affects the thermal diffusion resists the force-driven ballistic motion, *i.e.*, $\zeta^a \approx \zeta$. An example of this scenario in the simulations is the active dynamics with the smallest $f_0^a = 0.05\varepsilon/\sigma$ in Fig. 3.

The reduction of ζ^a with respect to ζ results from the strong activeness that makes the force-driven ballistic motion begins at $\tau^a_{\text{ballistic}} < \tau_d$. The ballistic motion with $\tau^a_{\text{ballistic}} < \tau_d$ renews the local environment of the nanorod at a rate that only allows the relaxation dynamics of chain segments with g^a monomers each to be complete, *i.e.*

$$\tau^a_{\text{ballistic}} \approx \tau^a_g \approx \tau_0 (g^a)^2 \tag{1}$$

where the monomeric time scale

$$\tau_0 \approx \frac{\eta_0 b^3}{k_B T} \tag{2}$$

The MSD of a force-driven active nanorod at $\tau^a_{\text{ballistic}}$ is comparable to the MSD of a passive nanorod at τ^a_g. For $t > \tau^a_{\text{ballistic}} \approx \tau^a_g$, the MSD due to the force-driven ballistic motion is above the MSD for the passive thermal motion, allowing the active nanorod to escape the effects of the relaxation dynamics of chain segments longer than g^a. As a result, for the force-driven active nanorod, the maximum viscosity corresponding to unscreened hydrodynamic interactions is

$$\eta^a_{\text{max}} \approx \eta_0 g^a \tag{3}$$

The effective viscosity using the rule of geometric mean is

$$\eta^a_{\text{eff}} \approx (\eta_0 \eta^a_{\text{max}})^{1/2} \approx \eta_0 (g^a)^{1/2} \tag{4}$$

The friction coefficient is

$$\zeta^a \approx \eta^a_{\text{eff}} l \tag{5}$$

which is smaller than ζ for the passive dynamics. A typical example of this scenario is the active dynamics with $f_0^a = 0.3\varepsilon/\sigma$ in Fig. 3.

For a large f_0^a that makes $\tau^a_{\text{ballistic}} \approx \tau^a_g < \tau_d$, we calculate the friction coefficient ζ^a of a force-driven active nanorod by matching the MSDs for the active and passive motion at $\tau^a_{\text{ballistic}} \approx \tau^a_g$. The constant speed of the force-driven ballistic motion

$$v^a = \frac{f^a}{\zeta^a} \tag{6}$$

where

$$f^a = f_0^a \left(\frac{l}{b}\right) \tag{7}$$

The MSD for the ballistic motion at $t \approx \tau^a_{\text{ballistic}} \approx \tau^a_g$ is

$$\langle \Delta r^2(\tau^a_g) \rangle^a_{\text{ballistic}} \approx (v^a \tau^a_g)^2 \tag{8}$$

The MSD for the passive thermal motion at $t \approx \tau^a_g$ is

$$\left\langle \Delta r^2 \left(\tau^a_g\right) \right\rangle^{\text{thermal}} \approx \left(\frac{k_B T}{\zeta^a}\right) \tau^a_g \tag{9}$$

where $k_B T/\zeta^a$ is the diffusion coefficient. From $\langle \Delta r^2(\tau^a_g) \rangle^a_{\text{ballistic}} \approx \langle \Delta r^2(\tau^a_g) \rangle^{\text{thermal}}$, we obtain the number of monomers per segment for the chain segments that affect the force-driven ballistic motion of the nanorod is

$$g^a \approx \left(\frac{f^a}{\mathscr{F}^a}\right)^{-4/3} \tag{10}$$

where

$$\mathscr{F}^a \approx \left(\frac{k_B T \eta_0 l}{\tau_0}\right)^{1/2} \approx \left(\frac{k_B T}{b}\right) \left(\frac{l}{b}\right)^{1/2} \tag{11}$$

As a result, the effective viscosity for the force-driven active nanorod is

$$\eta^a_{\text{eff}} \approx \eta_0 (g^a)^{1/2} \approx \eta_0 \left(\frac{f^a}{\mathscr{F}^a}\right)^{-2/3} \tag{12}$$

The corresponding friction coefficient is

$$\zeta^a \approx \eta^a_{\text{eff}} l \approx \zeta_0 \left(\frac{l}{b}\right) \left(\frac{f^a}{\mathscr{F}^a}\right)^{-2/3} \tag{13}$$

where the monomeric friction coefficient for the passive dynamics

$$\zeta_0 \approx \eta_0 b \tag{14}$$

Finally, the friction coefficient per monomer for the force-driven active nanorod is

$$\zeta^a_0 \approx \zeta^a / \left(\frac{l}{b}\right) \approx \zeta_0 \left(\frac{f^a}{\mathscr{F}^a}\right)^{-2/3} \approx \zeta_0 \left(\frac{f^a_0}{\mathscr{F}^a_0}\right)^{-2/3} \tag{15}$$

where

$$\mathscr{F}^a_0 = \mathscr{F}^a \Big/ \left(\frac{l}{b}\right) \tag{16}$$

Matching the two MSDs at τ^a_g corresponds to the work performed by the active force f^a at a speed v^a over a time of τ^a_g is comparable to the thermal energy $k_B T$, *i.e.*,

$$w^{a} \approx f^{a} v^{a} \tau_{g}^{a} \approx k_{B}T \tag{17}$$

which one can verify using eqn (1), (6), (10), (11), (13), and (14). Therefore, τ_{g}^{a} is the time scale above which the energy from the active force outcompetes the thermal energy $k_{B}T$. Recall that Einstein relation $D = k_{B}T/\zeta$ shows the diffusion coefficient for the passive dynamics is dictated by the thermal energy $k_{B}T$. Therefore, $w^{a} > k_{B}T$ for $t > \tau_{g}^{a}$ is consistent with the fact that the long-time ballistic motion of the force-driven nanorod is not affected by the thermal agitation. Likewise, the force $\mathscr{F}^{a}$ satisfies

$$\mathscr{W}^{a} \approx \mathscr{F}^{a} \mathscr{V}^{a} \tau_{0} \approx \mathscr{F}^{a} \left(\frac{\mathscr{F}^{a}}{\eta_{0} l}\right) \tau_{0} \approx k_{B}T \tag{18}$$

Eqn (18) means that $\mathscr{F}_{a}$ is a strong force at which the rod is coupled only to the monomer viscosity η_{0} with friction coefficient $\mathscr{L} \approx \eta_{0} l$, and the work $\mathscr{W}^{a}$ performed by $\mathscr{F}_{a}$ at the constant speed $\mathscr{V}^{a} \approx \mathscr{F}^{a}/\mathscr{L}$ over the monomer time scale τ_{0} is already comparable to the thermal energy $k_{B}T$.

The regime with the reduced friction coefficient ζ_{0}^{a} in eqn (15) occurs only when f_{0}^{a} is above the threshold $\tilde{f}_{0}^{a}$, at which the number of monomers per segment for the chain segments that affect the nanorod dynamics is

$$\tilde{g}^{a} \approx \begin{cases} (l/b)^{2}, & \text{if } l < R \\ N, & \text{if } l \geq R \end{cases} \tag{19}$$

where $R \approx N^{1/2} b$ is the average size of melt chains. Using eqn(10) for g^{a}, eqn (11) for $\mathscr{F}^{a}$, we obtain the active force at the threshold

$$\tilde{f}^{a} \approx \begin{cases} \mathscr{F}^{a}(l/b)^{-3/2} \sim (l/b)^{-1}, & \text{if } l < R \\ \mathscr{F}^{a} N^{-3/4} \sim (l/b)^{1/2} N^{-3/4}, & \text{if } l \geq R \end{cases} \tag{20}$$

As a result, the active force per monomer at the threshold

$$\tilde{f}_{0}^{a} \approx \begin{cases} \mathscr{F}_{0}^{a}(l/b)^{-3/2} \sim (l/b)^{-2}, & \text{if } l < R \\ \mathscr{F}_{0}^{a} N^{-3/4} \sim (l/b)^{-1/2} N^{-3/4}, & \text{if } l \geq R \end{cases} \tag{21}$$

where eqn (16) for $\mathscr{F}_{0}^{a}$ is used. Eqn (21) shows that as the rod length increases, there is a crossover from $\tilde{f}_{0}^{a} \sim l^{-2}$ to $\tilde{f}_{0}^{a} \sim l^{-1/2}$.

The scaling theory is compared with the simulation data for the systems with varying l and N. As shown in Fig. 5a, the plateau of ζ_{0}^{a} and the decrease of ζ_{0}^{a} with increasing f_{0}^{a} are observed in different simulation samples. The results for different l and N can be collapsed to a master curve

$$\frac{\zeta_{0}^{a}}{\zeta_{0}} = \left[1 + \left(\frac{f_{0}^{a}}{\tilde{f}_{0}^{a}}\right)^{2\beta/3}\right]^{-1/\beta} \tag{22}$$

that goes from the plateau regime $\zeta_{0}^{a}/\zeta_{0} = 1$ for $f_{0}^{a} < \tilde{f}_{0}^{a}$ to the power-law regime $\zeta_{0}^{a}/\zeta_{0} = \left(f_{0}^{a}/\tilde{f}_{0}^{a}\right)^{-2/3}$ for $f_{0}^{a} > \tilde{f}_{0}^{a}$ with β quantifying the shape of the curve at $f_{0}^{a} \approx \tilde{f}_{0}^{a}$. The exponent $-2/3$ in the power-law regime is the result of the scaling theory (eqn (15)). Fig. 5b shows the collapse of all simulation data points to the master curve. To obtain the master curve, ζ_{0}^{a}/ζ_{0} for different systems are simultaneously fit to eqn (22). The fitting result of β is 2.9 ± 0.6, and the best fit is used to construct the master curve (thick dashed line in Fig. 5b). The best-fit results of $\tilde{f}_{0}^{a}$ for different samples are shown in the inset to Fig. 5b and used to rescale the corresponding f_{0}^{a} to the master curve. The successful collapse of the data points in Fig. 5b validates the scaling theory for the power-law reduction of the friction coefficient with increasing strength of activeness (eqn (15)).

As shown in the inset to Fig. 5b, the l-dependence of $\tilde{f}_{0}^{a}$ for the force-driven active nanorods in the polymer melt of $N = 16$ exhibits a crossover from $\tilde{f}_{0}^{a} \sim l^{-2}$ to $\tilde{f}_{0}^{a} \sim l^{-1/2}$ as l increases from $l = 4\sigma$ slightly below $R \approx 4.7\sigma$ to $l = 32\sigma > R$. For the

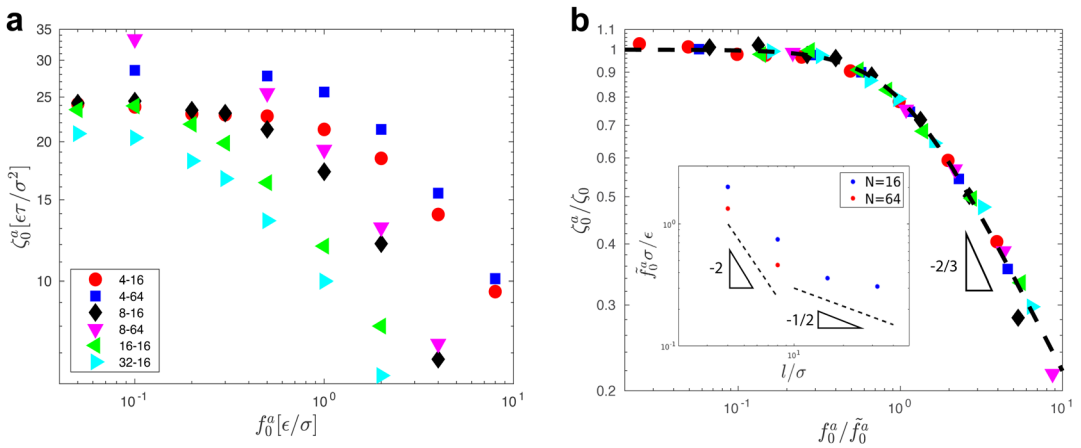

Fig. 5 (a) The monomeric friction coefficient ζ_{0}^{a} for the force-driven ballistic motion of an active thin nanorod in an unentangled polymer melt as a function of the active force per monomer f_{0}^{a}. The rod length l and the polymer melt chain length N are indicated in the format $l - N$. (b) Rescaling of ζ_{0}^{a} by the plateau value ζ_{0} and f_{0}^{a} by $\tilde{f}_{0}^{a}$, which is threshold active force for the reduction in ζ_{0}^{a}, results in the collapse of the data points in (a) to a master curve. The thick dashed line indicates the master curve (eqn (22)). The inset shows $\tilde{f}_{0}^{a}$ as a function of l for the nanorods in the melts of $N = 16$ and $N = 64$. The dashed lines in the inset indicate two scaling regimes in the theory.

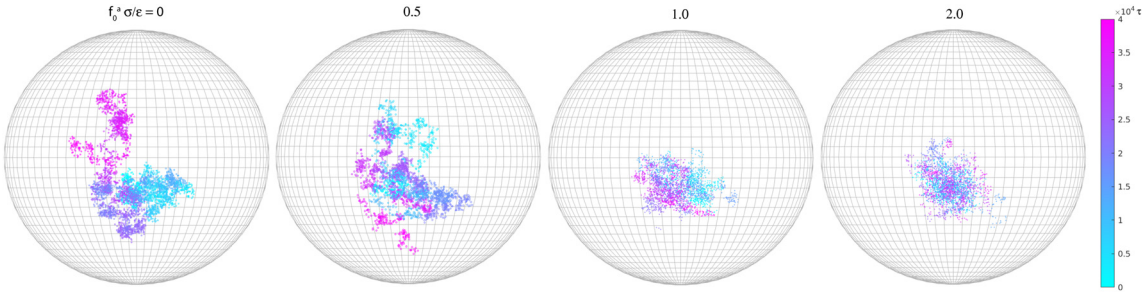

Fig. 6 Rotational trajectories of the unit vector $\vec{u}(t)$ along the rod axis for the force-driven active nanorods of $l = 32\sigma$ in polymer melts of $N = 16$.

nanorods in the other polymer melt of $N = 64$, $l = 4\sigma$ and $l = 8\sigma$ are both smaller than $R \approx 10.1\sigma$, and the l-dependence of $\tilde{f}_0^a$ is close to the scaling relation $\tilde{f}_0^a \sim l^{-2}$. These results agree with the scaling theory for the onset of the reduction in the friction coefficient (eqn (21)), further validating the theory.

Along with the decrease of ζ_0^a, there is a suppression of the rotation of the rod. We track the unit vector $\mathbf{u}(t)$ along the rod axis as a function of time, as visualized in Fig. 6. The range spanned by the tip of $\mathbf{u}(t)$ on the unit sphere decreases with increasing strength of the active force. The time-correlation function of the unit vector along the rod axis $\langle \mathbf{u}(t)\cdot\mathbf{u}(0)\rangle$ is computed. The results for the simulation samples in Fig. 6 are shown in Fig. 7. Here, as in the calculation of MSD (Fig. 3), the average is taken over different rods as well as different time periods of the same length in the steady state. For vanishing f_0^a, the correlation function approaches 0 over a time scale comparable to the rotational relaxation time $\tau_{rot} = 7.4 \times 10^4\tau$ for the passive thermal motion, which was obtained by fitting the decay of $\langle \mathbf{u}(t)\cdot\mathbf{u}(0)\rangle$ to $\exp(-t/\tau_{rot})$.[43] This indicates that the strength of the active force is weak and cannot keep the rod axis around its initial orientation or equivalently the force direction. As f_0^a increases, the correlation function levels off at a finite value up to the longest time scale in the simulations, indicating a stronger active force that suppresses the rotational diffusion of the rod axis. For the largest active force with $f_0^a = 2\varepsilon/\sigma$, the correlation function levels off at 0.93, indicating a much reduced rotational diffusion of the nanorod. The suppression of the rotational diffusion and the cutting off of the decorrelation of rod axis with time are consistent with the force-driven nanorod being coupled to local chain segments rather than entire polymer chains.

The reduction in rotational diffusion originates from the active force being in a fixed direction. If a self-propelled active force $f_0^a\mathbf{u}(t)$ were applied instead, the force would change its direction at timescales above the rotational relaxation time of the rod axis τ_{rot}. As a result, one would expect the terminal dynamics of the self-propelled active nanorod to be different from that with a constant driving force $f_0^a\mathbf{u}(0)$. Recent Brownian dynamics simulations of self-propelled active filaments[44] showed that the force-driven ballistic motion only persists to the timescale of τ_{rot}, after which the rotational diffusion of the filament randomizes the direction of self-propulsion, leading to a diffusive translational motion again.

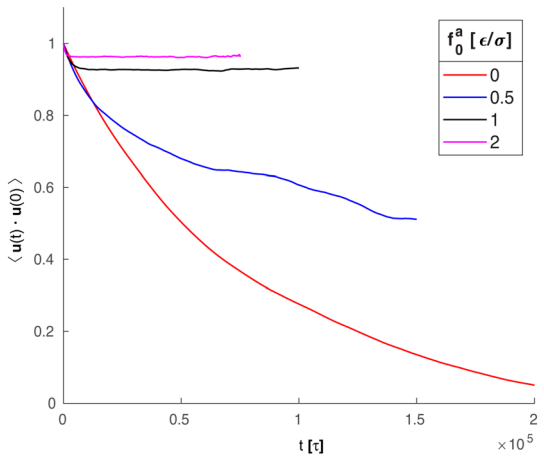

Fig. 7 Time-correlation function of the unit vector $\vec{u}(t)$ along the rod axis for the same systems in Fig. 6.

4 Concluding remarks

By combining molecular dynamics simulations and scaling theory analysis, we demonstrate the competition between the activeness induced by a constant external force and the passive thermal motion of the nanorod that is coupled to the viscosity of an unentangled polymer melt. The activeness outcompetes the thermal motion and results in a force-driven ballistic motion with a constant speed v^a in the force direction for the timescales above $\tau_{ballistic}$ (see Fig. 3). On the scaling level, $\tau_{ballistic}$ is the timescale where the work performed by the active force w^a is comparable to the thermal energy k_BT (eqn (17)). With increasing strength of the active force, $\tau_{ballistic}$ decreases below the terminal relaxation time τ_{melt} of entire polymer chains, allowing only the local viscosity of the chain segments with g^a monomers each and relaxation time $\tau_g^a \approx \tau_{ballistic} < \tau_{melt}$ to affect the force-driven active dynamics. As a result, the friction coefficient for the friction that balances the active force decreases with increasing strength of the active force (see Fig. 4). For sufficiently strong active force, the terminal speed v^a is above the thermal speed of the nanorod, and therefore the force-driven ballistic motion dominates all relevant time scales. Accompanying the reduction in the friction coefficient, the increase of the active force also leads to the suppression of

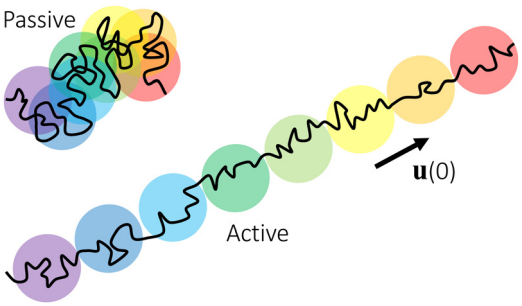

Fig. 8 Schematic illustration of the center-of-mass trajectories of thin nanorods (black lines) in unentangled polymer melts. The trajectory under an active force is a stretched array of active blobs (circles), which are segments of the trajectory over the time scale $\tau^{a}_{ballistic}$. Colors of increasing wavelength (from violet to red) are used to indicate the time order of the active blobs. The blobs of different colors overlap along the trajectory for the passive dynamics, indicating the randomness of the thermal diffusive motion. The arrow indicates the unit vector $\vec{u}(0)$ along the initial rod axis or equivalently the direction of the applied force.

the rotational diffusion of the rod and a strong correlation of the rod axis over time (see Fig. 6 and 7).

Regarding the connections to experiments,[28,29,62] the model of thin nanorods in the present work captures the effects of the anisotropic particle shape. Nevertheless, the model has yet to be extended to cover more aspects such as the rod thickness, which may be larger than the monomer length scale b, as well as the boundary conditions at the nanorod and polymer interface, which may involve attractive interactions between the rod and surrounding polymers and a grafted polymer brush layer that prevents the aggregation of nanorods. The steady-state motion of an active nanorod under constant external force as in the simulated model may be realized by the implementation of a nanorod with a uniformly distributed charge under an external electric field. Another way to extend the present computational and theoretical work to connect to a broader range of experiments is to include more disparate polymer matrices, such as entangled polymer melts, polymer solutions, and hydrogels.

Conceptually, the effect of the active force on the center-of-mass trajectory of a thin nanorod in an unentangled polymer melt may be compared with the effect of an external force on the conformation of a polymer chain. For a polymer chain with force of magnitude f applying at both chain ends, the random-walk conformation of an unperturbed chain is replaced by an extended array of tension blobs.[63] Each tension blob contains g monomers and the blob size $\xi \approx bg^{1/2}$ is the threshold length scale that chain segments are able to adopt the random-walk conformation without being perturbed by the external tensile force. The tension blob size is determined by $f\xi \approx kT$, reflecting the competition between the external perturbation and the thermal energy. Similarly, for a thin nanorod under the active force of magnitude f^{a}, the center-of-mass random-walk trajectory in the time domain for the passive dynamics of the nanorod is replaced by an extended array of "active blobs", as illustrated in Fig. 8. Each active blob corresponds to a time scale $\tau^{a}_{ballistic} \approx \tau^{a}_{g}$ (eqn (1)) and a length scale that is comparable to the MSD $\langle \Delta r^2(\tau^{a}_{g})\rangle^{a}_{ballistic} \approx (v^{a}\tau^{a}_{g})^2$ (eqn (8)). The random-walk trajectory at time scales below τ^{a}_{g} is not perturbed by the active force and follows the MSD for the thermal motion of the nanorod. τ^{a}_{g} and hence $\langle \Delta r^2(\tau^{a}_{g})\rangle^{a}_{ballistic}$ are determined by $w^{a} \approx f^{a}v^{a}\tau^{a}_{g} \approx k_{B}T$ (eqn (17)), which is a balance between the external perturbation and the thermal energy. Note that the random-walk trajectories for the passive dynamics and for the force-driven active dynamics at timescales below $\tau^{a}_{ballistic}$ are not ideal 3-dimensional random walks, as the translational diffusion along the rod axis is faster than that normal to the rod axis.[43] The description of the active dynamics trajectories using the language of blobs in polymer physics, as illustrated in Fig. 8, may provide a new perspective on the theory of active particles and active polymers.[64]

The microscopic insights provided by the molecular simulations and scaling theory may aid in the control of nanorods in functional nanorod–polymer composites using external force fields[65] and the manipulation of the trajectories of one-dimensional nanomotors in the applications of bio-imaging and drug delivery.[27] Additionally, the microscopic insights may also help understand the active filaments propelled by motor proteins in the cytoskeleton, RNA and DNA molecules in the transcription process within a cell, and also rod-like bacteria and viruses in biological settings.[64,66,67]

Author contributions

S. Zhang: methodology, software, formal analysis, investigation, data curation, visualization, review and editing of the manuscript; J. Wang: methodology, software, formal analysis, investigation, validation, and review and editing of the manuscript; T. Ge: conceptualization, supervision, writing – original draft preparation, and funding acquisition.

Conflicts of interest

There are no conflicts to declare.

Acknowledgements

T. G. acknowledges start-up funds from the University of South Carolina. This work was supported in part by the National Science Foundation EPSCoR Program under NSF Award No. OIA-1655740. Any opinions, findings and conclusions or recommendations expressed in this material are those of the authors and do not necessarily reflect those of the National Science Foundation. This work is partially supported by an ASPIRE grant from the Office of the Vice President for Research at the University of South Carolina. Simulations were performed on the flagship computing cluster Hyperion at the University of South Carolina.

Notes and references

1 M. Moniruzzaman and K. I. Winey, *Macromolecules*, 2006, **39**, 5194–5205.

2 H. Koerner, J. Kelley, J. George, L. Drummy, P. Mirau, N. S. Bell, J. W. Hsu and R. A. Vaia, *Macromolecules*, 2009, **42**, 8933–8942.
3 N. McCook, B. Boesl, D. Burris and W. Sawyer, *Tribol. Lett.*, 2006, **22**, 253–257.
4 J. Shen, X. Li, L. Zhang, X. Lin, H. Li, X. Shen, V. Ganesan and J. Liu, *Macromolecules*, 2018, **51**, 2641–2652.
5 A. Brioude, X. Jiang and M. Pileni, *J. Phys. Chem. B*, 2005, **109**, 13138–13142.
6 P. K. Jain, S. Eustis and M. A. El-Sayed, *J. Phys. Chem. B*, 2006, **110**, 18243–18253.
7 M. J. Hore, A. L. Frischknecht and R. J. Composto, *ACS Macro Lett.*, 2012, **1**, 115–121.
8 W. U. Huynh, J. J. Dittmer and A. P. Alivisatos, *Science*, 2002, **295**, 2425–2427.
9 S. I. White, B. A. DiDonna, M. Mu, T. C. Lubensky and K. I. Winey, *Phys. Rev. B*, 2009, **79**, 024301.
10 S. I. White, R. M. Mutiso, P. M. Vora, D. Jahnke, S. Hsu, J. M. Kikkawa, J. Li, J. E. Fischer and K. I. Winey, *Adv. Funct. Mater.*, 2010, **20**, 2709–2716.
11 R. M. Mutiso, M. C. Sherrott, J. Li and K. I. Winey, *Phys. Rev. B*, 2012, **86**, 214306.
12 R. M. Mutiso, M. C. Sherrott, A. R. Rathmell, B. J. Wiley and K. I. Winey, *ACS Nano*, 2013, **7**, 7654–7663.
13 X. Xu, H. Li, D. Hasan, R. S. Ruoff, A. X. Wang and D. L. Fan, *Adv. Funct. Mater.*, 2013, **23**, 4332–4338.
14 X. Yu, Y. Li, J. Wu and H. Ju, *Anal. Chem.*, 2014, **86**, 4501–4507.
15 B. Esteban-Fernández De Ávila, A. Martín, F. Soto, M. A. Lopez-Ramirez, S. Campuzano, G. M. Vásquez-Machado, W. Gao, L. Zhang and J. Wang, *ACS Nano*, 2015, **9**, 6756–6764.
16 S. Fu, X. Zhang, Y. Xie, J. Wu and H. Ju, *Nanoscale*, 2017, **9**, 9026–9033.
17 D. Kagan, R. Laocharoensuk, M. Zimmerman, C. Clawson, S. Balasubramanian, D. Kang, D. Bishop, S. Sattayasamitsathit, L. Zhang and J. Wang, *Small*, 2010, **6**, 2741–2747.
18 Z. Wu, X. Lin, X. Zou, J. Sun and Q. He, *ACS Appl. Mater. Interfaces*, 2015, **7**, 250–255.
19 M. Yu, J. Wang, Y. Yang, C. Zhu, Q. Su, S. Guo, J. Sun, Y. Gan, X. Shi and H. Gao, *Nano Lett.*, 2016, **16**, 7176–7182.
20 P. Díez, B. Esteban-Fernández De Ávila, D. E. Ramírez-Herrera, R. Villalonga and J. Wang, *Nanoscale*, 2017, **9**, 14307–14311.
21 B. Esteban-Fernández De Ávila, D. E. Ramírez-Herrera, S. Campuzano, P. Angsantikul, L. Zhang and J. Wang, *ACS Nano*, 2017, **11**, 5367–5374.
22 J. Wang and X. Shi, *Acta Mech. Solida Sin.*, 2017, **30**, 241–247.
23 M. Hansen-Bruhn, B. E. F. de Ávila, M. Beltrán-Gastélum, J. Zhao, D. E. Ramírez-Herrera, P. Angsantikul, K. Vesterager Gothelf, L. Zhang and J. Wang, *Angew. Chem., Int. Ed.*, 2018, **57**, 2657–2661.
24 J. Wang, Y. Yang, M. Yu, G. Hu, Y. Gan, H. Gao and X. Shi, *J. Mech. Phys. Solids*, 2018, **112**, 431–457.
25 C. Bao, B. Liu, B. Li, J. Chai, L. Zhang, L. Jiao, D. Li, Z. Yu, F. Ren and X. Shi, *Nano Lett.*, 2020, **20**, 1352–1361.
26 W. Bao, F. Tian, C. Lyu, B. Liu, B. Li, L. Zhang, X. Liu, F. Li, D. Li and X. Gao, *Sci. Adv.*, 2021, **7**, eaba2458.
27 J. Guo and Y. Lin, *Biomater. Transl.*, 2020, **1**, 18–32.
28 S. Alam and A. Mukhopadhyay, *Macromolecules*, 2014, **47**, 6919–6924.
29 J. Choi, M. Cargnello, C. B. Murray, N. Clarke, K. I. Winey and R. J. Composto, *ACS Macro Lett.*, 2015, **4**, 952–956.
30 S.-J. Li, H.-J. Qian and Z.-Y. Lu, *Phys. Chem. Chem. Phys.*, 2018, **20**, 20996–21007.
31 A. Karatrantos, R. J. Composto, K. I. Winey and N. Clarke, *Macromolecules*, 2019, **52**, 2513–2520.
32 K. I. Morozov and A. M. Leshansky, *Macromolecules*, 2022, **55**, 3116–3128.
33 W. Gao, S. Sattayasamitsathit, K. M. Manesh, D. Weihs and J. Wang, *J. Am. Chem. Soc.*, 2010, **132**, 14403–14405.
34 D. L. Fan, R. C. Cammarata and C. L. Chien, *Appl. Phys. Lett.*, 2008, **92**, 093115.
35 Y. Wang, R. M. Hernandez, D. J. Bartlett, J. M. Bingham, T. R. Kline, A. Sen and T. E. Mallouk, *Langmuir*, 2006, **22**, 10451–10456.
36 W. Gao, A. Uygun and J. Wang, *J. Am. Chem. Soc.*, 2012, **134**, 897–900.
37 M. Manjare, B. Yang and Y. P. Zhao, *J. Phys. Chem. C*, 2013, **117**, 4657–4665.
38 X. Ma, A. C. Hortelao, A. Miguel-López and S. Sánchez, *J. Am. Chem. Soc.*, 2016, **138**, 13782–13785.
39 Z. Huang, P. Chen, G. Zhu, Y. Yang, Z. Xu and L.-T. Yan, *ACS Nano*, 2018, **12**, 6725–6733.
40 F. B. Wyart and P. G. de Gennes, *Eur. Phys. J. E: Soft Matter Biol. Phys.*, 2000, **1**, 93.
41 M. Doi and S. F. Edwards, *The theory of polymer dynamics*, Oxford University Press, 1988.
42 J. Happel and H. Brenner, *Low Reynolds number hydrodynamics: with special applications to particulate media*, Martinus Nijhoff: The Hague, 1983.
43 J. Wang, T. C. O'Connor, G. S. Grest, Y. Zheng, M. Rubinstein and T. Ge, *Macromolecules*, 2021, **54**, 7051–7059.
44 S. Mandal, C. Kurzthaler, T. Franosch and H. Löwen, *Phys. Rev. Lett.*, 2020, **125**, 138002.
45 C. Kurzthaler, S. Mandal, T. Bhattacharjee, H. Löwen, S. S. Datta and H. A. Stone, *Nat. Commun.*, 2021, **12**, 7088.
46 K. Kremer and G. S. Grest, *J. Chem. Phys.*, 1990, **92**, 5057–5086.
47 G. S. Grest, *J. Chem. Phys.*, 2016, **145**, 141101.
48 H.-P. Hsu and K. Kremer, *J. Chem. Phys.*, 2016, **144**, 154907.
49 S. Lu, Z. Wu and A. Jayaraman, *J. Phys. Chem. B*, 2021, **125**, 2435–2449.
50 S. Lu and A. Jayaraman, *ACS Macro Lett.*, 2021, **10**, 1416–1422.
51 S. Plimpton, *J. Comput. Phys.*, 1995, **117**, 1–19.
52 A. P. Thompson, H. M. Aktulga, R. Berger, D. S. Bolintineanu, W. M. Brown, P. S. Crozier, P. J. in 't Veld, A. Kohlmeyer, S. G. Moore, T. D. Nguyen, R. Shan, M. J. Stevens, J. Tranchida, C. Trott and S. J. Plimpton, *Comput. Phys. Commun.*, 2022, **271**, 108171.

53 L.-H. Cai, S. Panyukov and M. Rubinstein, *Macromolecules*, 2011, **44**, 7853–7863.
54 L.-H. Cai, S. Panyukov and M. Rubinstein, *Macromolecules*, 2015, **48**, 847–862.
55 T. Ge, J. T. Kalathi, J. D. Halverson, G. S. Grest and M. Rubinstein, *Macromolecules*, 2017, **50**, 1749–1754.
56 T. Ge, G. S. Grest and M. Rubinstein, *Phys. Rev. Lett.*, 2018, **120**, 057801.
57 T. Ge and M. Rubinstein, *Macromolecules*, 2019, **52**, 1536–1545.
58 U. Yamamoto and K. S. Schweizer, *J. Chem. Phys.*, 2011, **135**, 224902.
59 J. T. Kalathi, U. Yamamoto, K. S. Schweizer, G. S. Grest and S. K. Kumar, *Phys. Rev. Lett.*, 2014, **112**, 108301.
60 U. Yamamoto and K. S. Schweizer, *Macromolecules*, 2015, **48**, 152–163.
61 C. Aponte-Rivera and M. Rubinstein, *Macromolecules*, 2021, **54**, 1783–1800.
62 K. A. Rose, M. Molaei, M. J. Boyle, D. Lee, J. C. Crocker and R. J. Composto, *J. Appl. Phys.*, 2020, **127**, 191101.
63 M. Rubinstein and R. H. Colby, *Polymer Physics*, Oxford University Press, 2003.
64 R. G. Winkler and G. Gompper, *J. Chem. Phys.*, 2020, **153**, 040901.
65 M. J. Hore and R. J. Composto, *Curr. Opin. Chem. Eng.*, 2013, **2**, 95–102.
66 M. Smith, R. Poling-Skutvik, A. H. Slim, R. C. Willson and J. C. Conrad, *Macromolecules*, 2021, **54**, 4557–4563.
67 G. C. L. Wong, J. D. Antani, P. P. Lele, J. Chen, B. Nan, M. J. Kühn, A. Persat, J.-L. Bru, N. M. Høyland-Kroghsbo, A. Siryaporn, J. C. Conrad, F. Carrara, Y. Yawata, R. Stocker, Y. V. Brun, G. B. Whitfield, C. K. Lee, J. de Anda, W. C. Schmidt, R. Golestanian, G. A. O'Toole, K. A. Floyd, F. H. Yildiz, S. Yang, F. Jin, M. Toyofuku, L. Eberl, N. Nomura, L. A. Zacharoff, M. Y. El-Naggar, S. E. Yalcin, N. S. Malvankar, M. D. Rojas-Andrade, A. I. Hochbaum, J. Yan, H. A. Stone, N. S. Wingreen, B. L. Bassler, Y. Wu, H. Xu, K. Drescher and J. Dunkel, *Phys. Biol.*, 2021, **18**, 051501.